Journal of Hydrology: Regional Studies 30 (2020) 100699

Contents lists available at ScienceDirect

Journal of Hydrology: Regional Studies

journal homepage: www.elsevier.com/locate/ejrh

Numerical study of the thermal structure of a stratified temperate monomictic drinking water reservoir

Fuxin Zhang[a,b], Hong Zhang[a,b,*], Edoardo Bertone[a,b], Rodney Stewart[a,b], Charles Lemckert[c], Kathy Cinque[d]

[a] School of Engineering and Built Environment, Griffith University, Queensland, 4222, Australia
[b] Cities Research Institute, Griffith University, Queensland, 4222, Australia
[c] School of Design and the Built Environment, University of Canberra, Bruce, ACT, 2617, Australia
[d] Melbourne Water, 990 LaTrobe St., Docklands, VIC, 3008, Australia

ARTICLE INFO

Keywords:
Hydrodynamic modelling
Stratification
Schmidt stability
Tarago Reservoir

ABSTRACT

Study region: Tarago Reservoir, Victoria, Australia.
Study focus: This study investigates the influence of rainfall, river inflow and wind on the temperature stratification of the Tarago Reservoir by incorporating atmospheric and bathymetric conditions using a three-dimensional hydrodynamic model.
New hydrological insights for this region: In this study, a three-dimensional (3D) hydrodynamic model was developed and applied to the Tarago Reservoir. The model allowed 3D visualization of the thermal structure, and the seasonal and longitudinal differences in stratification could be quantified using the Schmidt stability index. The simulation results revealed longitudinal differences in thermal structure among the riverine, transition, and lacustrine zones. The bathymetry affects the lake stratification and stability; furthermore, the strong vertical current caused by the sharp bathymetry gradient significantly weakens the stability in deep zones. In addition, this study assessed the impacts of rainfall and wind on lake stability using sensitivity analysis. The results indicated that rainfall decreases the water temperature of the lake but hardly affects the summer stratification. Moreover, the wind not only influences the intensity and duration of stratification but also contributes to the heat storage of waterbodies. The patterns of water current velocities and temperature also showed that the circulation generated by overflow and underflow plumes have a crucial effect on the thermal structure of the transition and lacustrine zones.

1. Introduction

The reservoirs in Australia have a combined water capacity of more than 91,000 G L and are collection and storage systems for domestic, irrigation, and industrial use as well as for flood control. More than 20 temperate reservoirs store approximately 2000 G L of water in Victoria and South Australia. These reservoirs develop a cycle of thermal stratification and mixing every year. In addition to external factors such as heat exchange and wind force, the changes in the thermal structure of these reservoirs are directly subject to internal influences such as lake morphometry (Han et al., 2000; Helfer et al., 2009).

* Corresponding author at: School of Engineering and Built Environment, Griffith University, Queensland, 4222, Australia.
E-mail addresses: Fuxin.zhang@griffithuni.edu.au (F. Zhang), hong.zhang@griffith.edu.au (H. Zhang), r.stewart@griffith.edu.au (R. Stewart), charles.lemckert@canberra.edu.au (C. Lemckert), kathy.cinque@melbournewater.com.au (K. Cinque).

https://doi.org/10.1016/j.ejrh.2020.100699
Received 12 February 2020; Received in revised form 24 April 2020; Accepted 24 May 2020

Numerous researchers have investigated the thermal structure of lakes and reservoirs and suggested that physical, chemical, and biological processes in aquatic environments affect the stratification and mixing process (Helfer et al., 2011; Kirillin and Shatwell, 2016; Lawson and Anderson, 2007; Yu et al., 2014a). When stratification develops in a temperate monomictic reservoir (i.e., reservoirs that mix once a year), the vertical thermal dynamics of the reservoir present remarkable changes (Noori et al., 2019). Boehrer and Schultze (2008) and Imboden and Wüest (1995) revealed that the processes affecting heat transfer through the surface layer of reservoirs include short wave radiation from the sun, longwave radiation of the atmosphere and surface waters, sensible heat exchange, and heat flux caused by evaporation and precipitation. These processes exert a rather limited influence upon the deep layers, especially in hypereutrophic lakes where algae grow abundantly; furthermore, heat transport from the surface to deeper layers relies mainly on turbulence and wind-induced currents (Sundaram and Rehm, 1971). The different thermal dynamics between the surface layer and deep layers cause a considerable change in water temperature, and the differences in water density caused by these temperature differences produce positive buoyancy gradients. The stability of such gradients is affected by the combined action of wind-induced stirring and convection from surface cooling when turnover occurs (Kirillin, 2010).

As engineered structures, reservoirs possess morphological features that differ from those of natural lakes. In general, reservoirs are long and narrow; have a main inflow with many tributaries and an outflow at or near the dam wall; and can be divided into three distinct zones: riverine, transition, and lacustrine, reflecting the obvious longitudinal differences in morphological, hydrodynamic, and water-quality properties (Ji, 2017). Water temperature differences between the inflow and reservoir water cause opposite movements of the inflow current. Referred to as 'thermocline erosion', this condition significantly influences the temperature distribution of the transition and lacustrine zones (Hebbert et al., 1979). Therefore, a comprehensive analysis of thermal structure requires a three-dimensional (3D) water-temperature distribution in reservoirs. Field measurements of water temperature can usually only be acquired at several observation points; however, these measurements are not sufficient to visualise and understand spatial and temporal variations in the thermal structure of entire reservoirs because of the frequent changes in the heat exchange and flow regime as well as the longitudinal difference in reservoirs' morphological features.

Over the past two decades, the application of numerical modelling in the study of lakes and reservoirs has experienced remarkable progress and played an extensive and unique role in revealing the inherent movements within waterbodies (Chao et al., 2010; Yu et al., 2014b; Zhang and Chan, 2003). Numerical modelling has widely been considered an appropriate tool for simulating the hydrodynamic characteristics of various waterbodies (Antonopoulos and Gianniou, 2003; Hostetler and Bartlein, 1990; Patterson and Imberger, 1989). Previous studies have adopted vertical one-dimensional (1D) hydrodynamic models to simulate the cycle of thermal stratification and mixing in lakes, and have highlighted that atmospheric heat exchange, incoming solar radiation, and wind forcing play vital roles in the thermal structure of waterbodies (Bertone et al., 2015; MacKay et al., 2009; Tuan et al., 2009). Given the limitations of 1D models, most of these studies have focused on vertical temporal variations of the thermal structure at one specific location of a reservoir; research focusing on the relationship between thermal behaviours and spatial variations is rare. For nearly 20 years, 3D numerical modelling has exhibited great potential as a method for investigating the spatial variation of the thermal structure in reservoirs (Lessin et al., 2014; Torriano et al., 2012). León et al. (2007) simulated surface fluxes, thermal structure, and hydrodynamic components in Great Slave Lake, Canada and conducted a series of sensitivity analyses based on meteorological inputs through a 3D hydrodynamic model. Li et al. (2018) successfully simulated the hydrodynamics and thermal dynamics of Poyang Lake, China through 3D numerical models and revealed significant spatial variability of the thermal stability. A combined 3D hydrodynamic model and watershed model was published by Dargahi and Setegn (2011). The model presented the characteristics of the summer stratification profile and dominant factors affecting thermal structures. The aforementioned research studies have provided strong evidence that 3D numerical models are effective and reliable tools for analysing the thermal structure of natural waters. However, to the authors' knowledge, research focusing specifically on the influence of morphological differences on the thermal structure and hydrodynamic characteristics caused by the significant differences among riverine, transition, and lacustrine zones is limited.

The Tarago Reservoir in Victoria, Australia, presents significant longitudinal differences in morphology and experiences a distinct seasonal variation in water temperature. As the main water supply for Westernport and the Mornington Peninsula in Victoria, Australia, the water quality of the Tarago Reservoir is critical to the health of local residents. However, the reservoir has experienced some water quality issues since its establishment in 1969, and Tarago Water Treatment Plant (TWTP) was constructed to deal with the deteriorating water quality of the reservoir in 2009 (Young, 2009). Without a comprehensive understanding of the variation in the reservoir's thermal structure, it is difficult to predict the pollutant transport in it. Consequently, high-efficiency and low-cost water treatment cannot be guaranteed at all times. The challenges associated with treating seasonally deteriorated raw water may lead to complaints from consumers. Therefore, investigating the temporal and spatial variation in the thermal structure is vital for water resources management.

The goals of this study were to investigate the thermal structure of the Tarago Reservoir; the influence of rainfall and wind on the thermal structures in the riverine, transition, and lacustrine zones; and the role of overflow and underflow during stratification. The present study developed and validated a 3D numerical model for the reservoir. The simulation results provided visualised hydrodynamic and thermodynamic processes of the reservoir. Based on the spatial pattern of the Schmidt stability index (SSI), the temporal and spatial differentiation of the thermal structure variation were revealed. Furthermore, the roles of rainfall and wind were examined through comparisons of simulated results from the model with different scenarios. The pattern of water temperature and current velocities revealed the roles of overflow and underflow during stratification.

Fig. 1. (**a**) Geographical map of Tarago Reservoir (38°1′S 145°56′E) and its water-supply district; (**b**) Surface appearance of the Tarago Reservoir (A: Neerim south station; B: Tarago Reservoir station). (Data source: Geoscience Australia).

2. Study site and materials

2.1. Research domain

The Tarago Reservoir (38°1′S 145°56′E, Fig. 1(a)) is approximately 85 km east of Melbourne in Victoria, Australia, and has a maximum capacity of 37,580 mL of freshwater. It was built in 1969 to supply drinking water to the Mornington Peninsula and Westernport (Fig. 1(a)), which in 2016 had a population of 165,000 (Australian Bureau of Statistics, 2016). The surface area of the reservoir is approximately 360 ha and its catchment area is 11,400 ha. The maximum depth of the reservoir is approximately 23 m near the dam wall. Upstream of the reservoir is the Tarago River and on average 60 mL of water is transported into the Tarago Reservoir per day. The average annual evaporation and precipitation from 2012 and 2017 were 1751 mm and 857 mm, respectively. The average air temperature for the reservoir is 13.73 °C, and the lowest daily air temperature from 2012 to 2017 is 2.75 °C. With a mean volume of 22,548 mL and a mean annual inflow of 0.36 m^3/s, the hydraulic retention time of the reservoir is 1.97 years. The morphological features of the Tarago Reservoir are in line with the three abovementioned zones, namely the riverine, transition, and lacustrine zones. The shape of the reservoir is narrow and long and its water depth gradually increases from the main inflow to outflow, reaching its maximum near the dam.

The Tarago Reservoir experienced significant algal blooms in the early 1990s, and its outflows were removed from the urban water supply system because of poor water quality. The Melbourne area suffered persistent low rainfall, famously referred to as the 'Millennium Drought', where the water storage in the area dropped to 38.9 % of the total capacity in December 2006 and 25.5 % in June 2009. In 2009, the TWTP was built to purify the outflows from the reservoir, which allowed it to be reconnected to the water-supply system. However, seasonal factors have led to some periods with high manganese, which has created challenges for plant operations.

2.2. Monitoring data

Melbourne Water provided the bathymetry of the Tarago Reservoir. The discharge of the inflow and outflow and the meteorological conditions of the Reservoir, such as air temperature, wind speed, wind direction, relative humidity, clearness, and precipitation (Table 1), were observed at Neerim South Station and Tarago Reservoir Station (Fig. 1(b)), which are managed by the Australian Bureau of Meteorology (BoM). In addition, Melbourne Water provided rough records about the temperature of the water samples that were collected in the Tarago River, the inflow of the reservoir. In 2017, the Vertical Profiling System (VPS) structure was installed by Melbourne Water in the region near the dam wall (Fig. 1(b)), and since then it has been collecting a series of parameters

Table 1
Meteorological data and boundary conditions from June 2017 to June 2018.

Category	Parameters	Date source	Frequency
Meteorological conditions	Air temperature (°C)	Neerim South Station	Hourly
	Wind speed (m/s)	Neerim South Station	Hourly
	Wind direction (°)	Neerim South Station	Hourly
	Precipitation(mm)	Neerim South Station	Daily
	Evaporation (mm)	Neerim South Station	Daily
	Relative humidity	Australian BoM	Monthly
	Clearness	Australian BoM	Monthly
Boundary conditions	Inflow water temperature (°C)	Melbourne Water sampling	Monthly
	Inflow water discharge (m^3/s)	Neerim South Station	Daily
	Outflow water temperature (°C)	Tarago Reservoir Station	3-hly
	Outflow water discharge (m^3/s)	Tarago Reservoir Station	Daily

including water temperature and water level at a three-hour frequency and a one-meter vertical. The high-frequency vertical water temperature records were of crucial significance for the calibration and validation of the hydrodynamic model. All data collected in this study are available for the period from June 2017 to June 2018.

3. Methodology

3.1. 3D hydrodynamic model

This study adopted the DHI MIKE 3 Flow Model to simulate the temporal and spatial behaviours of thermal structure through the simulation of flow dynamics and heat exchange in the Tarago Reservoir (DHI, 2017). The MIKE 3 Flow Model, a non-hydrostatic numerical-modelling system, has been successfully employed in various hydrodynamic studies in oceans, coasts, estuaries, and lakes (Kheirabadi et al., 2018; Ma et al., 2009; Sokolova et al., 2013; Vo and Gourbesville, 2016). The fundamental component of this flow model is its hydrodynamic module, which simulates unsteady 3D flows based on density variations, bathymetry, and external forces such as meteorology, currents, and other hydrographic conditions. The mathematical foundations of the model are as follows: the mass conservation equation; 3D Reynolds-averaged Navier–Stokes equations including the effect of turbulence and variable density; and a conservation equation for temperature and salinity.

For the purposes of the modelling study, an accurate description of heat exchange was required. Heat exchange is calculated based on the sensible heat flux, latent heat flux (evaporative heat loss), net shortwave radiation, and net longwave radiation. The four physical processes were calculated using an embedded heat exchange module, and most parameters have been specified in MIKE3 (DHI, 2017). The intensity of solar radiation was described as a function that depends on the distance to the sun, declination angle and latitude, extraterrestrial radiation, and the cloudiness and amount of water vapour in the atmosphere (Henderson-Sellers, 1986; Imberger and Hamblin, 1982; Tucker, 1982; Weisman and Brutsaert, 1973). The evaporative heat loss determined by Dalton's law is given by Eq. (1). As the equation shows, the constants a_1 and b_1, called Constant and Wind coefficient in Dalton's law, respectively, must be specified. The evaporation rate can be calculated from the latent heat flux using Eq. (2):

$$q_v = LC_e(a_1 + b_1 W_{2m})(Q_{water} - Q_{air}) \tag{1}$$

$$\Delta\eta_e = -\frac{q_v}{L\rho_{water}} \tag{2}$$

where L is the latent heat of vaporisation, $2.5{\cdot}10^6$ J/kg; C_e is the moisture coefficient, $1.32{\cdot}10^{-3}$; W_{2m} is the wind speed 2 m above the sea surface; Q_{water} is the water vapour density close to the surface; Q_{air} is the water vapour density in the atmosphere; and $\Delta\eta_e$ is the evaporation rate.

3.1.1. Bathymetry and grid

Melbourne Water provided details of the bathymetry of the study site (see Fig. 2). This domain of the Tarago Reservoir was converted to a grid map with parameters (see Table 2). The relative altitude of the surrounding land in the grid map was defined as 10 m. The depth given by a grid point represents both the grid and the surrounding area, which weakens the topographical change of the bottom of the reservoir. Spacing of 0.5 m was adopted in the vertical direction to ensure a high resolution of simulated vertical temperature profiles. Fig. 2 also shows the two open boundaries of the reservoir inflow in the north and the outflow in the south.

3.1.2. Boundary conditions

The boundary conditions included the water discharge and water temperature at the Neerim South Station and the Tarago Reservoir Station. The shoreline of Tarago Reservoir was defined as an impermeable and zero normal velocity boundary. Furthermore, the inflow water temperature was assumed to be constant in the vertical direction. However, as Table 1 demonstrates, the frequency (monthly) of the inflow water temperature is insufficient to represent the temperature variation. Thus, this study used

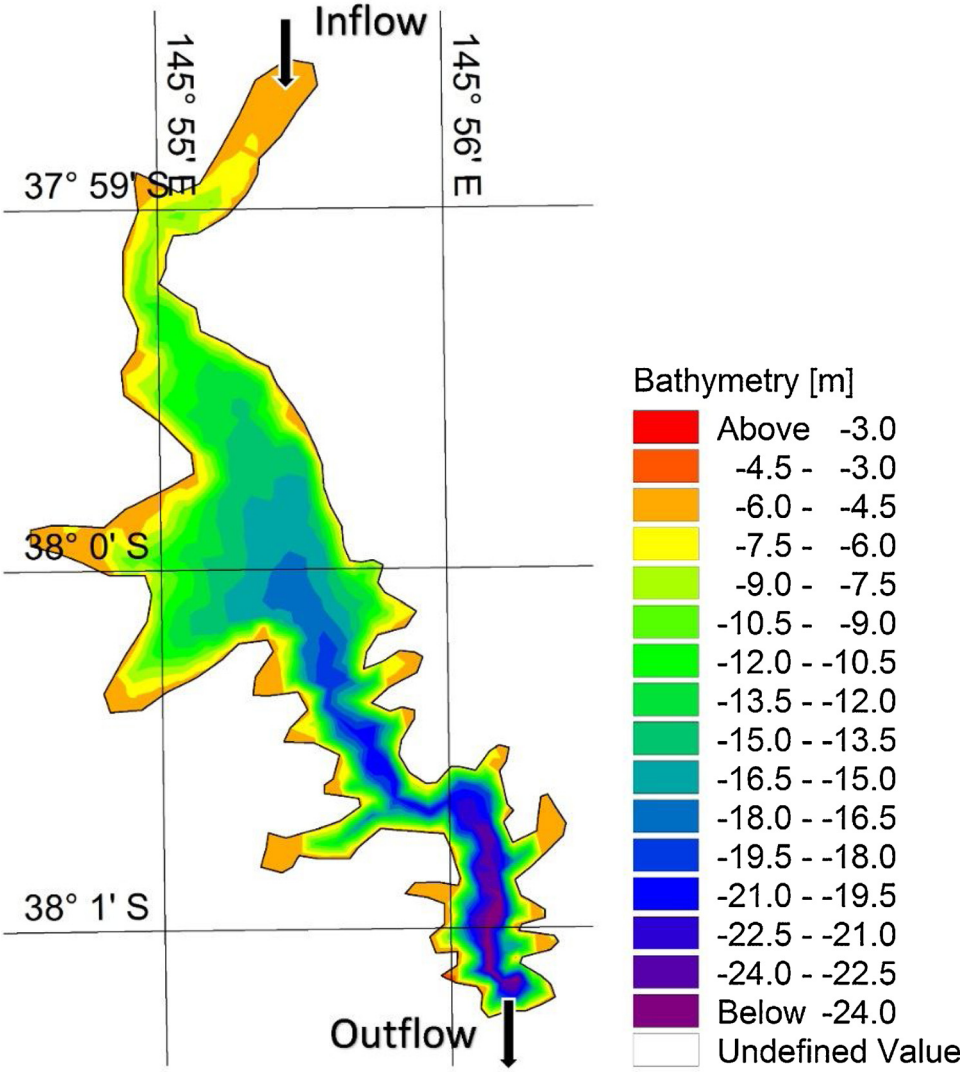

Fig. 2. Bathymetry of the Tarago Reservoir.

Table 2
Setting parameters of the grid map.

Map projection	UTM-55	
Geographical origin coordinated	Longitude 145.908726	Latitude −38.020580
X-axis	Grid number: 68	Grid Space: 40 m
Y-axis	Grid number: 120	Grid Space: 40 m
Z-axis	Grid number: 46	Grid Space: 0.5 m

the correlation between air temperature and water temperature from August 2005 to September 2009 (Fig. 3) to estimate the daily inflow water temperature. Moreover, this study adopted the linear regression model for one dependent variable (air temperature) to estimate the water temperature (Webb and Nobilis, 1997). The simple model is given by Eq. (3):

$$T_w(t) = A + BT_a(t) + \varepsilon(t) \tag{3}$$

where $T_w(t)$ is the water temperature for a given day; $T_a(t)$ is the air temperature for the same day as water temperature; A and B are regression parameters; and $\varepsilon(t)$ is an error term.

The parameters A and B were determined through the curve fitting between local air temperature (T_a) and inflow water temperature (T_w). The R-squared of 0.8163 indicated that the estimation of the inflow water temperature on air temperature is feasible,

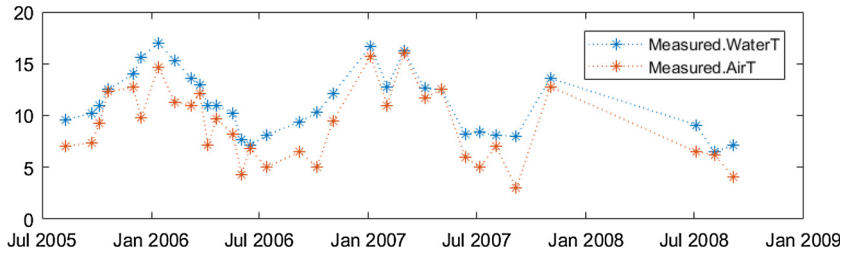

Fig. 3. Measured water and air temperatures from 2005 to 2009.

and parameters A and B were 0.77 and 4.26, respectively. Fig. 5 presents the discharge and water temperature of the inflow and outflow of the Tarago Reservoir during the study period. The historical discharge records indicated that neither inflow nor outflow discharges exhibited a seasonal change.

3.1.3. Model setup

The model defined the density variation as the function of salinity and water-temperature variation and considered detailed meteorological conditions. Local air temperature, wind speed and direction, and precipitation were collected hourly at the Tarago Reservoir Station. The clearness coefficient is bright sunshine hours divided by the length of the day, where 100 % specifies a clear sky and 0% specifies cloudy weather. Relative humidity is the amount of moisture in the air as a percentage of the amount of moisture the air can actually contain. Average monthly clearness was 66 % from December 2016 to May 2017 and 45 % for the rest of the research period. The average monthly relative humidity was 75 % for the entire research period. The initial water temperature was set at 10.75 °C at the starting time of 00:00, 31 August 2017 when the reservoir was in a well-mixed condition, which was effective for minimizing the vertical error in water temperature. The simulation period of this model was from 31 August 2017 to 1 June 2018 to ensure that the simulation would experience entire stratification and mixing processes. Given the numerical stability restriction of this model, the simulated interval was specified as 20 s. Notably, the model required four weeks to finish the modelling 'warm-up' because a 'cold start' was adopted, which initialised the velocity field to zero at the beginning of the simulated period.

The heat-exchange coefficients (see Table 3) were calibrated using the measured water temperature. The turbulence module is a mixed k-ε/Smagorinsky model that includes various empirical constants and diffusion parameters, which were obtained from prior reported experimental results (Horiuti, 1987). The Smagorinsky coefficient and eddy viscosity limits were specified in the turbulence model (Table 3). In addition, a linear relationship was assumed between the dispersion of temperature and the eddy viscosity, which was defined by the dispersion factor and dispersion limits (Table 3). In addition, the wind friction factor is calculated in accordance with Smith and Banke (1975).

The data collected by the VPS provide three-hourly measurements for water temperatures from the surface (depth = 1 m) to a depth of 14 m with 1-m vertical spacing. The validation of the model was undertaken through a comparison between the measured and simulated water temperatures using the time series and vertical profiles. The mean absolute error (MAE) and root mean square

Table 3
Parameters used in model setup.

Model component	Model parameters	Value	Note
Heat-exchange coefficients	Constant in Dalton's law, a_1	1.2	Calibrated
	Wind coefficient in Dalton's law, b_1	0.5	Calibrated
	Sun constant, a in Ångstrøm's law	0.229	Default
	Sun constant, b in Ångstrøm's law	0.572	Default
	Beta in Beer's law	0.3	Calibrated
	Light extinction coefficient	1.5	Calibrated
	Standard meridian for time zone	147	
Turbulence module coefficient	Smagorinsky horizontal coefficient	0.28	Sokolova et al. (2013)
	Eddy viscosity limits in horizontal	1	Calibrated
	Eddy viscosity limits in vertical	0.001	Calibrated
Dispersion coefficients	Horizontal dispersion factor	1.0	Calibrated
	Vertical dispersion factor	0.2	Calibrated
	Dispersion limit in horizontal	0.02	Calibrated
	Dispersion limit in vertical	0.1	Calibrated
Wind condition	Wind friction coefficient linear variation		
	Wind speed	0 − 12 m/s	
	Wind friction coefficient	0.0016 − 0.0026	Calibrated
Resistance	Bed roughness	0.005	Default

error (RMSE) were used to detect the performance of the model. In addition, Pearson's product-moment correlation coefficient (R) or R^2, the coefficient of determination, is usually used to describe the correlation between simulated and observed data (Legates and McCabe, 1999); the square of R ranges from 0 to 1, with values close to 1 indicating a better correlation. In addition, this study introduced the index of agreement developed by Willmott (Willmott, 1981) to provide comparisons of the simulated data (P) with the observed data (O). The advantage of the index of agreement is its ability to give the proper weight to the error and difference; however, the distinct disadvantage of this index is that it exaggerates the influence of the extreme values (Legates and McCabe, 1999). Given that there were hardly any extreme values in the simulated results, the index of agreement was more valuable than the square of R. The index of agreement is given by

$$d = 1 - \frac{\sum_{i=1}^{N}(O_i - P_i)^2}{\sum_{i=1}^{N}(|P_i - \bar{O'}| + |O_i - \bar{O'}|)^2} \tag{4}$$

where P is the simulated data; O is the observed data; $\bar{O'}$ is the weighted mean direction or vector of the elements contained in the observed data; N is the sum of elements contained in the observed data; and i is the number of the element.

3.2. Stratification-stability analysis

This research adopted the SSI to quantify the degree of mixing and stratification to enable a more detailed understanding of spatial and temporal variations in thermal structure (Read et al., 2011). Schmidt stability was defined by Schmidt (1928) to reflect the resistance to mechanical mixing caused by the potential energy of the water column during stratification. The SSI has been widely used to indicate the stability of the water column and describe the intensity of thermal stratification in waterbodies (Bertone et al., 2015; Kirillin and Shatwell, 2016; Lawson and Anderson, 2007; Li et al., 2018). The SSI was given by

$$S_T(x, y) = g\int_0^{z_D}\left(z - \frac{z_D}{2}\right)(\rho_z(x, y, z) - \rho(\bar{x}, y)\partial z \tag{5}$$

where g is the gravity acceleration [m/s^2]; ρ_z is the density at depth z and $\bar{\rho}$ is the mean density of the water column; z_D is the maximum depth of the lake [m]; and z_v is the depth to the centre of the water column, [m].

4. Results and discussion

4.1. Validation of simulated water level and temperature

The outputs of the MIKE 3 Flow Model provided simulated water temperatures at a 0.5-m vertical interval every hour. The measured water level and water temperature from the VPS (see Fig. 1) were used to validate the model. Two time series of simulated and observed water levels at the sample station indicated that the simulated results agreed with the variation and trend of the observed data (Fig. 6). Fig. 7 presents the time series of the observed and simulated water temperatures at the surface and middle layers. Table 4 presents the MAE, RMSE, coefficient of determination (R^2), and the index of agreement in the comparisons between the observed and simulated water temperatures at the surface (depth = 1 m) and middle (depth =8 m) layers. The mean absolute errors and RMSE for all layers were low and less than 1.0 °C. The high coefficient of determination (R^2) and index of agreement indicated the simulated temperatures agreed well with observations.

To validate the model's capability to simulate the vertical distribution of water temperature, the vertical profiles of the simulated and measured water temperatures were compared at 12 moments, which included the diurnal and seasonal changes in water temperature. Fig. 8 demonstrates that the simulated results closely matched the measured results, representing a high level of consistency between the simulated and measured data. The simulated results accurately reproduced not only the vertical distribution of water temperature but also the daily and seasonal variation of temperature gradients from strong stratification to the mixing condition.

The simulated water temperature after mid-March was slightly lower than the observed value. Similarly, the model underestimated the water level when the reservoir was in a mixing condition. In Table 4, the RMSE, R^2 and Index of agreement indicates that the model reproduced the overall trend of the surface water temperature well, but Fig. 7 shows deficiencies in simulating the surface water temperature on short time scales. The constant coefficients used in the heat exchange module, such as the Constant and Wind coefficients in Dalton's law, Beta in Beer's law, and the light extinction coefficient, guaranteed efficient and reliable operation but reduced the accuracy of numerical simulations at short time scales. In addition, the monthly records of clearness and humidity were not sufficient. These drawbacks affected the performance of the model; however, in general, the validation results indicated

Table 4
Index of the comparisons between the measured and simulated values.

	Depth 1 m	Depth 4m	Depth 8 m	Depth 15 m
MAE (°C)	0.558	0.446	0.447	0.444
RMSE (°C)	0.689	0.595	0.535	0.614
R^2	0.963	0.920	0.970	0.949
Index of agreement	0.986	0.943	0.987	0.966

high model accuracy.

4.2. Simulated thermal structure

Although the water temperature measured by the VPS could not provide an overall understanding of the thermal structure of the Tarago Reservoir, it contributed to the calibration and validation of the 3D model. This study investigated the thermal structure of the reservoir through the simulation results of the water temperature of the entire reservoir. To reveal the spatial difference of thermal structure during the simulated period, three locations in the reservoir were chosen to represent the riverine, transition, and lacustrine zones (see Fig. 9). The maximum depths of the three locations were 8, 12, and 22 m, respectively. The simulated vertical temperature distributions of these locations from September 2017 to June 2018 are displayed in Fig. 9, which shows a complete cycle of stratification and turnover occurring in the reservoir. Furthermore, the figure demonstrates that depth is a crucial factor causing the difference in the thermal structure. The boundary between the stratification and mixing condition in the riverine zone is blurry because the water temperatures on the bottom increased rapidly. The stratification lasted a relatively short time and was broken in early January 2018. In Fig. 9(b), it is obvious that the deep layers of the transition zone continued warming from December 2017 to early February 2018, and the period when water temperatures were in a continuously increasing trend was longer and extended to early March 2018 in the lacustrine zone. Consequently, the duration of stratification increased with rising depth. In addition, the date of turnover caused by the drop in air temperature was identified in early April 2018. However, the water temperature of the entire water column became almost uniform between March and April, which suggested a significant reduction in the gradient of water density. Hence, the deterioration of water quality caused by the mixing process might have occurred before turnover. The time series of vertical water temperature distribution clearly reflected the temporal variation of the thermal structure in several locations in the reservoir, but it was impractical to analyse the spatial difference of thermal structure through the time series. Therefore, the SSI was introduced for this purpose.

4.3. Stratification stability

Based on the calculation of the SSI in Eq. (5), exploration of the seasonal differences in thermal structure in the riverine, transition, and lacustrine zones became feasible. The spatial pattern of the monthly SSI in the Tarago Reservoir was calculated from the density, in turn computed from the validated MIKE 3 Flow Model. The SSI pattern of the different seasons—September 2017 for spring, December 2017 for summer, March 2018 for autumn, and June 2018 for winter—are presented in Fig. 10.

Several previous studies undertaken on reservoirs and lakes of substantially different sizes have indicated that an SSI value of 200 J/m^2 is a sensible threshold for ensuring thermal stratification (Li et al., 2018; Magee and Wu, 2017; Read et al., 2011). In Fig. 10(b), which presents the summer of 2018, the Schmidt stability in most regions with a depth more than 12 m exceeded 200 J/m^2, and the index of the shallow area near shore and inlet varied from only 50 J/m^2 to 150 J/m^2. The SSI of regions A and C exceeded 350 J/m^2, which represented the regions with the strongest stratification during summer. As Fig. 10(a) and (d) demonstrate, the SSI of the entire reservoir hardly exceeded 100 J/m^2, and the index of any area other than region C (Fig. 10(b)) was rarely more than 50 J/m^2. The SSI became very low during spring and winter even in the lacustrine zones, which indicated that the thermal structure of the Tarago Reservoir in spring and winter tends to be weak and susceptible to mixing.

Comparing Fig. 10 and the bathymetry (Fig. 2), the SSI gradually increased with the increasing water depth from the inlet to the outlet, reaching its peak at the deepest area near the dam (region C). Therefore, it is obvious that a gradually increasing depth along the flow direction is correlated to an increase in Schmidt stability. However, the SSI in region B (Fig. 10(b)), where an abrupt and narrow curve between region A and C is present, remained at a relatively low level compared with nearby values. A significant decrease in Schmidt stability indicated that the 'sharp turn' influenced the thermal structure of zone B. Here, the current dynamic is a key to interpreting the mechanism of the 'sharp turn' for the stratification. Four spots with similar depths (Fig. 11(a)) were chosen as targets to examine the change in current velocity and the vertical velocity component from spot A to D. The simulated results from the validated model provided the current velocities and velocity components in the vertical direction. This study calculated the mean of the absolute value of current velocity and the vertical velocity (w-velocity) component in December 2017. Fig. 11(b) and (c) display the vertical profiles of these mean absolute velocities. The magnitude of current velocities of the four spots was similar, but the magnitude of the vertical velocity component in spot A was significantly greater than those in the other three, especially in the layers below a depth of 5 m. This difference demonstrates that the vertical movement of current is much more significant at the 'sharp turn' than it is in spots B, C, and D, and led to the reduction of the stability of thermal stratification during December 2017.

To summarise, the stratification stability of the entire reservoir presents a significant seasonal change, and the depth of water mainly affects stratification stability during the same season. The longitudinal difference in stratification stability is particularly apparent during summer. In addition, the stratification stability in some deep zones can be significantly weakened by the 'sharp turn' because an active vertical current movement occurs there.

4.4. Effects of rainfall and wind

The total rainfall for the Tarago Reservoir was approximately 780 mm in 2018. Fig. 4 presents the daily precipitation in the Tarago Reservoir from September 2017 to June 2018, which indicated that heavy precipitation occurred at different times/seasons during the study period. To generate a simulation without the influence of rainfall, the rainfall condition was removed from the original 3D hydrodynamic model. Through comparing the new simulated results with the original ones, the role of rainfall on the

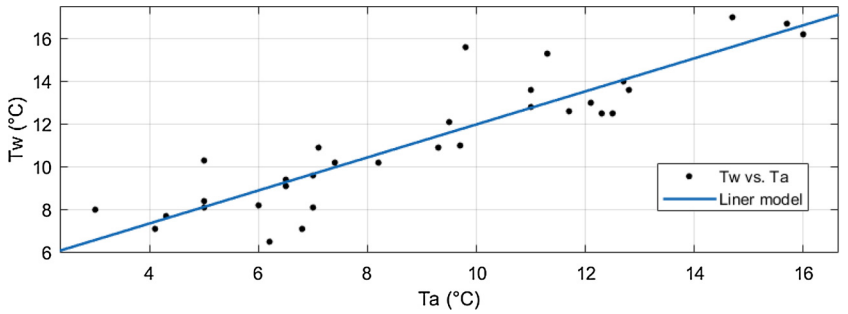

Fig. 4. Linear regression model for inflow water temperature.

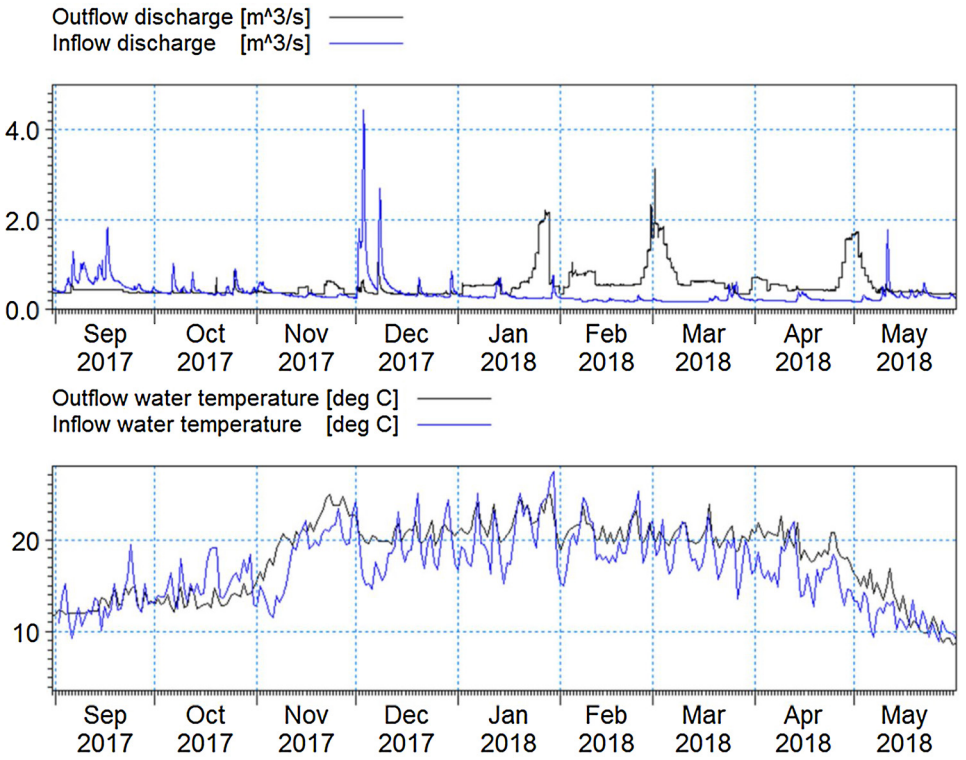

Fig. 5. Discharge and water temperature of the inflow and outflow from September 2017 to June 2018.

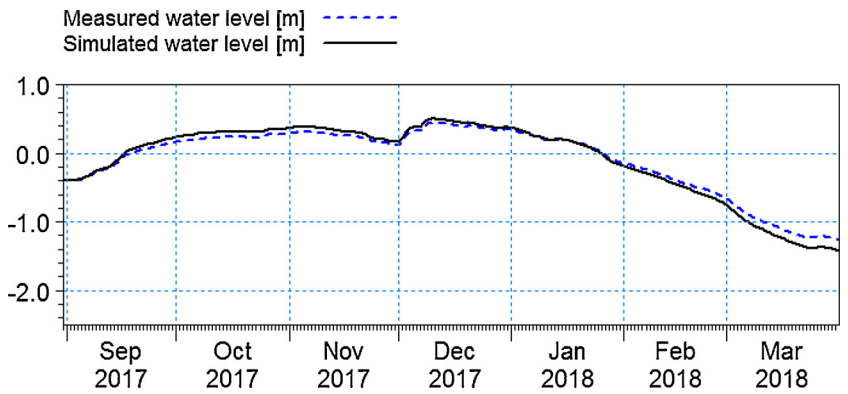

Fig. 6. Measured (dotted line) and modelled (solid line) water levels at the sample station.

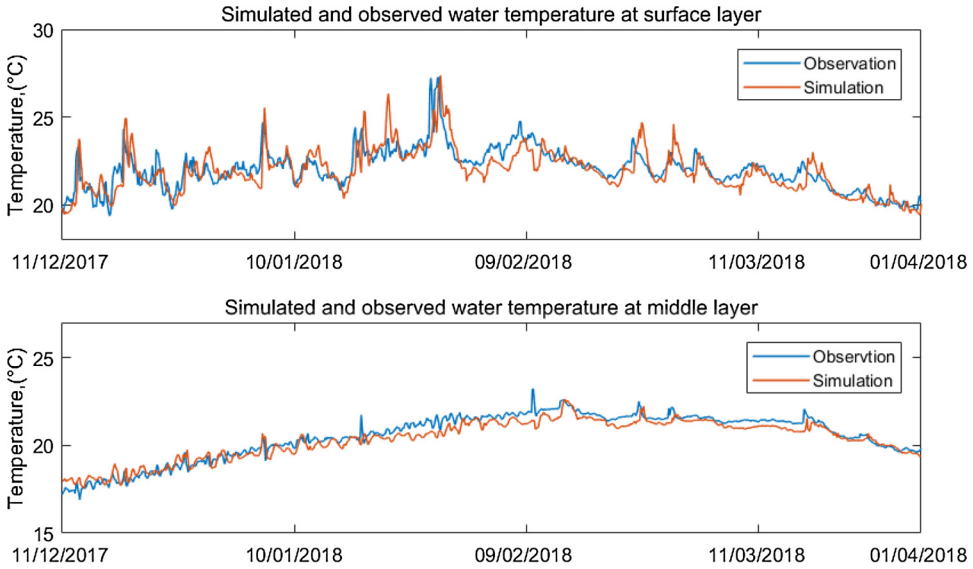

Fig. 7. Observed and simulated water temperatures at the surface and middle layers of the observation point from 11/12/2017 to 1/4/2018.

thermal structure was revealed.

Fig. 12 shows the vertical profiles of water temperature from two simulations in the three locations representing riverine, transition, and lacustrine zones (see Fig. 9) during heavy rainfall at 3:00 pm on 3rd, 4th and 5th December. The simulated water temperatures from the surface to 5 m in depth simulated by the model eliminating rainfall (no-rainfall model) were noticeably higher than those simulated by the original model. The gaps between two vertical profiles were greater in the epilimnion than in the hypolimnion and approached zero at the bottom of the reservoir. Therefore, the role of rainfall is more significant in the riverine zone than in the transition and lacustrine zones, mainly due to a lower depth leading to a thermal change throughout the profile, unlike in the deeper lacustrine zone. The input of heavy rainfall reduced the water temperature, especially in the epilimnion, and in view of the comparisons shown in Fig. 12, the rainfall had minimal impact on the stratification during days with the heaviest rainfall.

To check the difference in stratification for the two models during the entire research period, the SSI was used to quantify the structure of stratification. The relative difference in SSI (DSSI), which is used to illustrate the proportion of the influence of rainfall on the stratification, was described as follows:

$$DSSI = \frac{SSI_O - SSI_{NR}}{SSI_O} \tag{6}$$

where SSI_O is the SSI from original model results; SSI_{NR} is the SSI from no-rainfall model results.

Three time series of the DSSI are presented in Fig. 13, while the SSI from the original model was used to show the phase of stratification. The figure shows that the proportions of varying SSI due to rainfall were never more than 5% during summer stratification even in the riverine zone. When SSI dropped to a very low level in the mixing process, a slight change of SSI caused a significant DSSI and the relative difference became meaningless. Xuan et al. (2015) observed that heavy rainfall with more than 160 mm/day caused the bottom water temperature to increase by approximately 4.0 °C and accelerated the mixing process. However, with the heaviest rainfall being less than 50 mm/day in the Tarago Reservoir, rainfall exhibited a minimal influence on the bottom water temperature. In view of the fact that the rainfall has never exceeded 50 mm/day in the Tarago Reservoir over the past decade, it can be concluded that the rainfall occurring there caused the water temperature to drop in the epilimnion but hardly influenced the thermal stratification. Future work is required to develop a rainfall-runoff model to ensure the inflow can also be adjusted according to the change in rainfall for different scenarios, thereby enabling the current results to be confirmed.

The wind force is a vital factor determining circulation and vertical mixing of the reservoir. A no-wind model provides a way to examine the thermal structure of the reservoir without wind, and thus assess how sensitive the model is (and the reservoir) to wind. Fig. 14 displays comparisons between the vertical profiles of water temperature simulated by original and no-wind models. Without the influence of wind, the water temperature of deep layers did not change; instead, sharper temperature gradients occurred in the epilimnion. The simulated results indicated that the heat flux could not reach the deep layers without wind forcing, and furthermore, the vertical mixing produced by wind is the principal driving force contributing to the downward transport of heat.

To further study the role of wind, two further hypothetical scenarios were analysed based on the field wind conditions: a strong wind scenario, which used 1.5 times the field wind speed, and a weak wind scenario, which used 0.5 times the field wind speed. Original wind directions were not altered. Fig. 15 displays the vertical profiles of water temperature simulated for the three scenarios. In the original event, the main phase of the formation and reinforcement of summer stratification was from 3/11/2017 to 3/01/2018, and the stratification was broken after 3/03/2018. Sharper temperature gradients occurring during the weak wind event indicated a more stable summer stratification and delayed destratification; by contrast, strong wind of 1.5 times the field wind speed caused

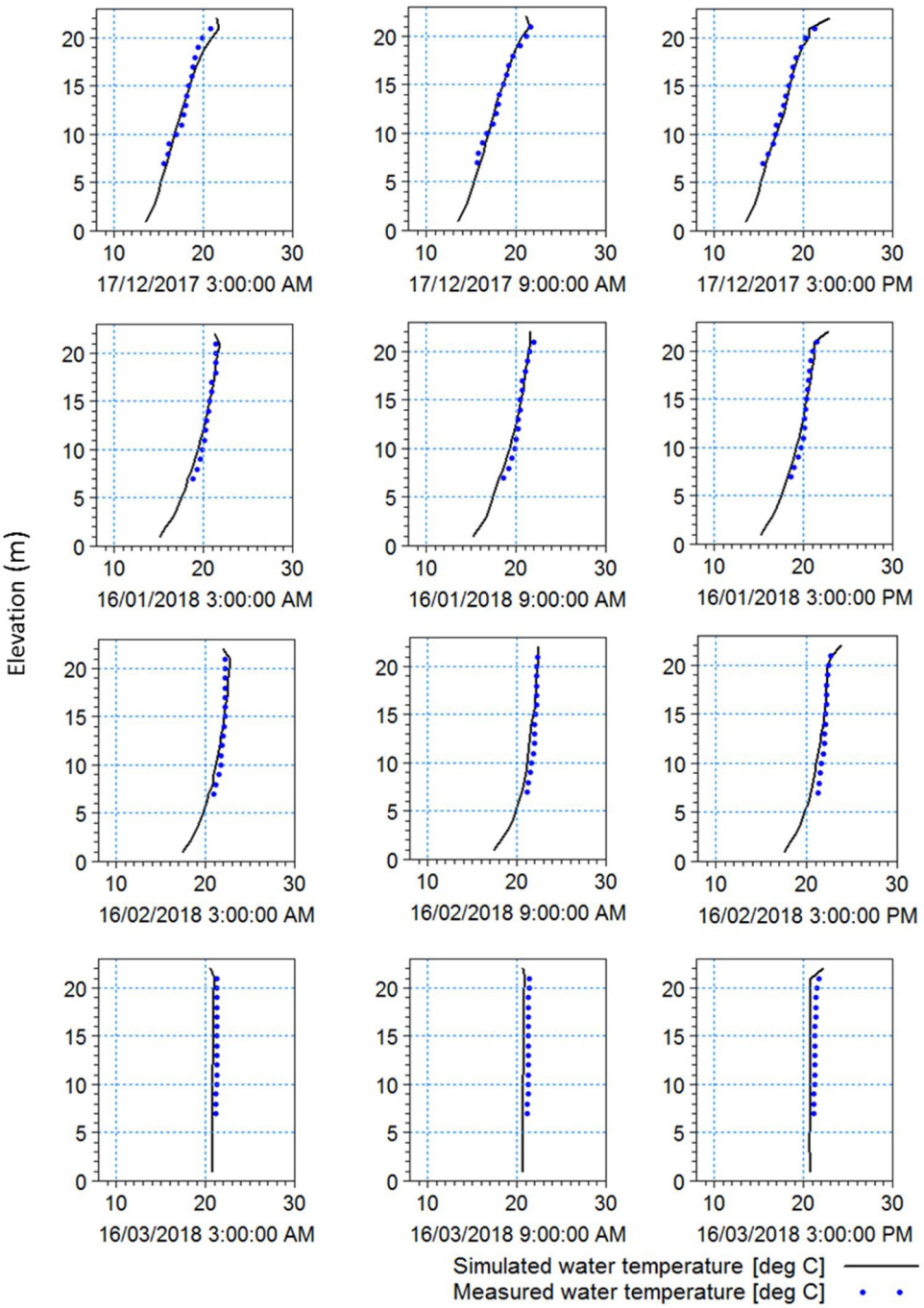

Fig. 8. Validation for vertical water-temperature profiles for seasonal periods representing stratification and mixing condition at the observation point.

stronger vertical mixing, which prevented the formation of a considerable stratification.

The wind conditions determined the rate of the downward transport of heat, and the rate was the key factor in the formation and destruction of the stratification. The difference in vertical temperature profiles among the riverine, transition, and lacustrine zones revealed that the thermal structure of the reservoir depends on both the maximum depth of the water column and wind conditions. The strong wind scenario suggested a very high rate of heat transport into deep layers. The shallow zones remained in mixing conditions during the mid-seasons, and only lacustrine zones a depth of approximately 20 m presented a mild stratification. The differences in thermal structure among the three zones were more distinct in the weak wind scenario, which also resulted in stronger stratification. For instance, the riverine zone with a depth of 7 m was in a mixing condition after 3/03/2018, but the transition and

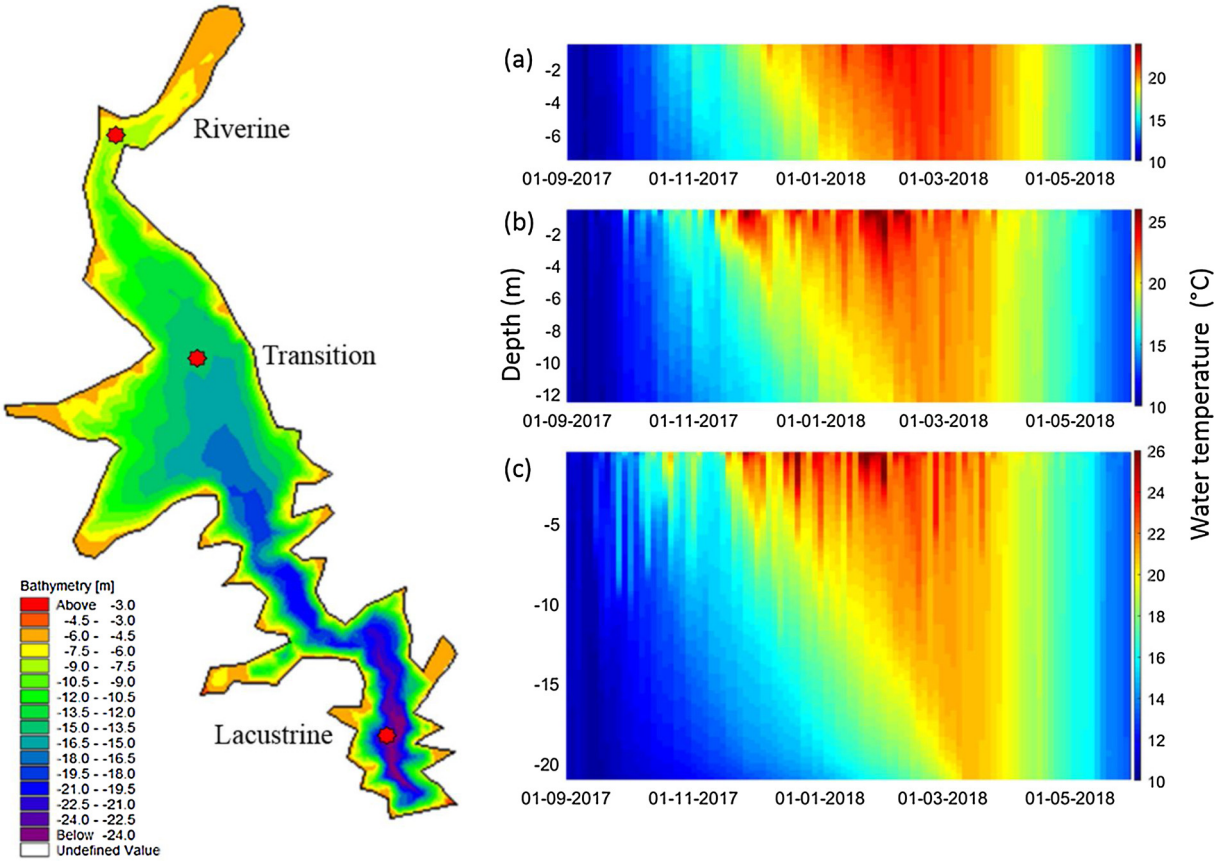

Fig. 9. Simulated vertical temperature distributions in (a) the riverine zone (maximum depth = 8 m); (b) the transition zone (maximum depth = 12 m); and (c) the lacustrine zone (maximum depth = 22 m) of the Tarago Reservoir from September 2017 to June 2018.

lacustrine zones were still in a steady stratification.

For these three scenarios, the waterbody eventually reached full mixing conditions and presented similar vertical profiles of water temperature. Compared with the vital role of wind conditions during stratification, the influence of wind after turnover can be neglected. In addition, the differences in temperature vertical profile indicated that wind conditions determine the capacity of the reservoir to store heat. Although strong wind causes evaporation resulting in heat loss, a very large amount of heat is transported and stored in the deep layers of the reservoir with the help of strong wind. In conclusion, wind condition plays a fundamental role in changing the thermal structure of the Tarago Reservoir. Furthermore, the degree and duration of stratification are related to the intensity of the wind conditions. The capacity of the reservoir to store heat also depends on the wind conditions. In view of the dominant role of wind in disturbing the summer stratification, strong wind conditions restrain the deterioration of hypolimnion water quality introduced by stable stratification but advance and strengthen the turnover. In addition, the annual total evaporation from the reservoir is strongly affected by the wind speed (1494 mm with 0.5 times field wind speed, 2082 mm with field wind speed, and 2670 mm with 1.5 times field wind speed). Increased evaporation causes the reservoir volume to decrease more rapidly, which in turn affects the thermal stability of the water column. Therefore, the effect of wind on the thermal structure of the reservoir is vital for water management.

4.5. Roles of cold and warm inflow plumes in stratification

Inflow plumes play a vital role in the heat input of reservoirs, and the temperature of inflow plumes determines their movement to a great extent when inserted into reservoirs. Given the different densities caused by temperature variation, the dynamic of an inflow plume presents a significant differentiation when a heat or cold inflow plume enters the reservoir. Theoretically, warm currents with lower density affect the surface flow dynamics, but cold currents tend to move downwards because of their higher densities (Han et al., 2000).

In the Tarago Reservoir, the hydraulic retention time is 1.97 years with a mean annual inflow of 0.36 m^3/s, and a flood event did not occur during the study period. The influences of the inflow boundary condition on the current dynamic and temperature of riverine zones were checked. Fig. 16 compares water temperatures between inflow boundary conditions and the three locations in the riverine zone (R1, R2, and R3 in Fig. 11). The water temperature at the three locations did not exhibit a similar trend or magnitude to

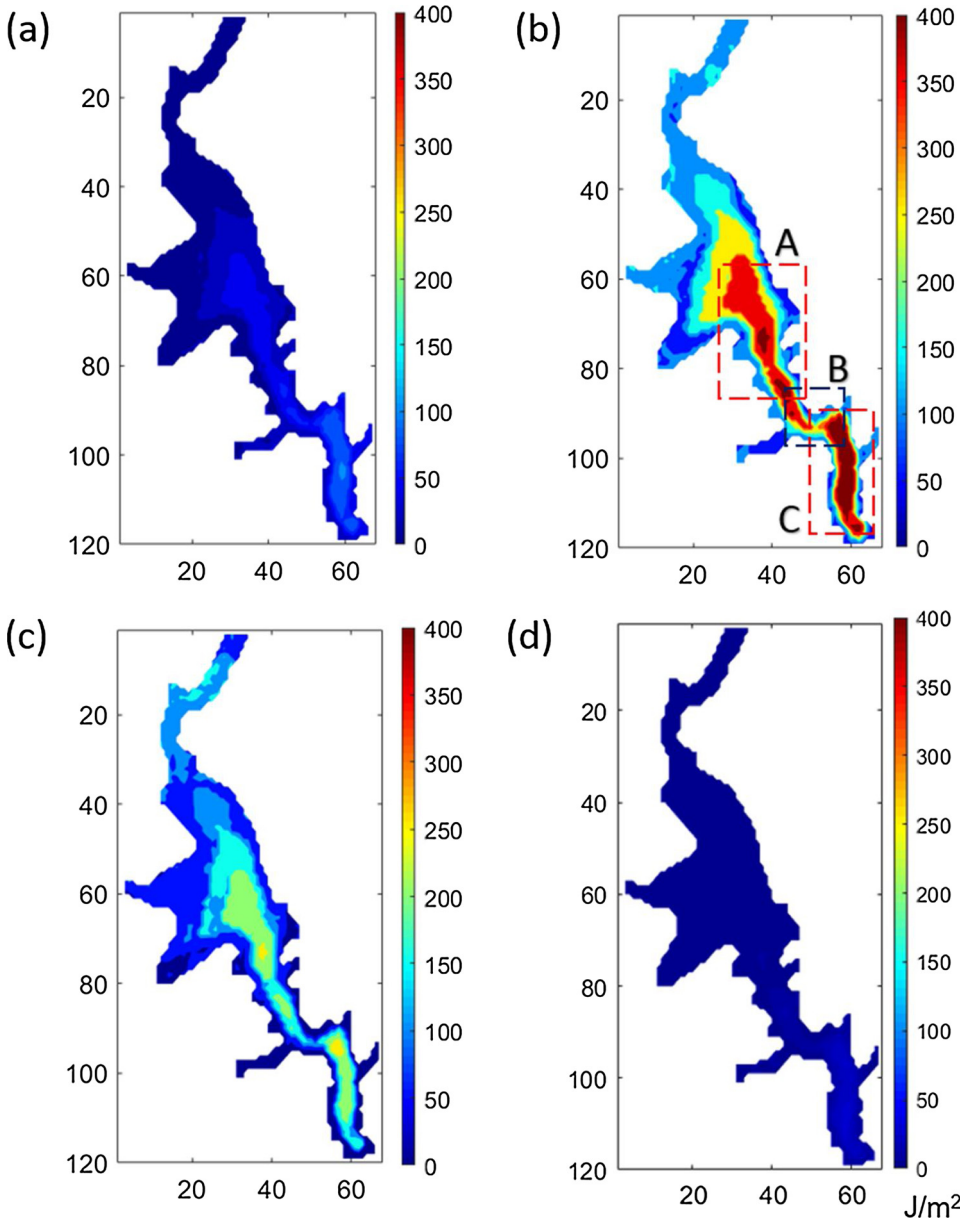

Fig. 10. Spatial pattern of monthly average Schmidt stability index values in the Tarago Reservoir in (a) September 2017; (b) December 2017; (c) March 2018; and (d) June 2018.

that of the inflow water temperature, which revealed that the inflow conditions had a negligible effect on the riverine zone. Therefore, subsequent analyses should not concentrate on the inflow boundary condition itself.

To further discuss the role of inflow on the thermal structure of the lacustrine zone, the 3D hydrodynamic model with a constant inflow water temperature (11.69 ˚C, the average value during the research period) was deployed. Fig. 17 presents a comparison of the original and new time series of water temperature at the point representing the lacustrine zone (see Fig. 9). The differences between the two simulated results were never more than 0.8 ˚C, which proved that the variation of inflow water temperature has a minimal effect on the thermal structure of the lacustrine zone. In view of the fact that the riverine zone occupies a quarter of the longitudinal length of the reservoir, the thermodynamic activities in the riverine zone are crucial to the thermal structure of the entire reservoir. Therefore, the definition of inflow in the analysis of intrusion flows was not limited to the boundary conditions but extended to the shallow area located in the riverine zones. The type of inflow depends on the water-temperature pattern of the riverine zones rather than on the inflow water temperature. Thus, the intrusion flows were divided into overflow and underflow according to the comparison of water temperatures between the riverine zones and transition zone.

Acquiring a comprehensive understanding of the roles of overflow and underflow plumes in the thermal structure in the Tarago

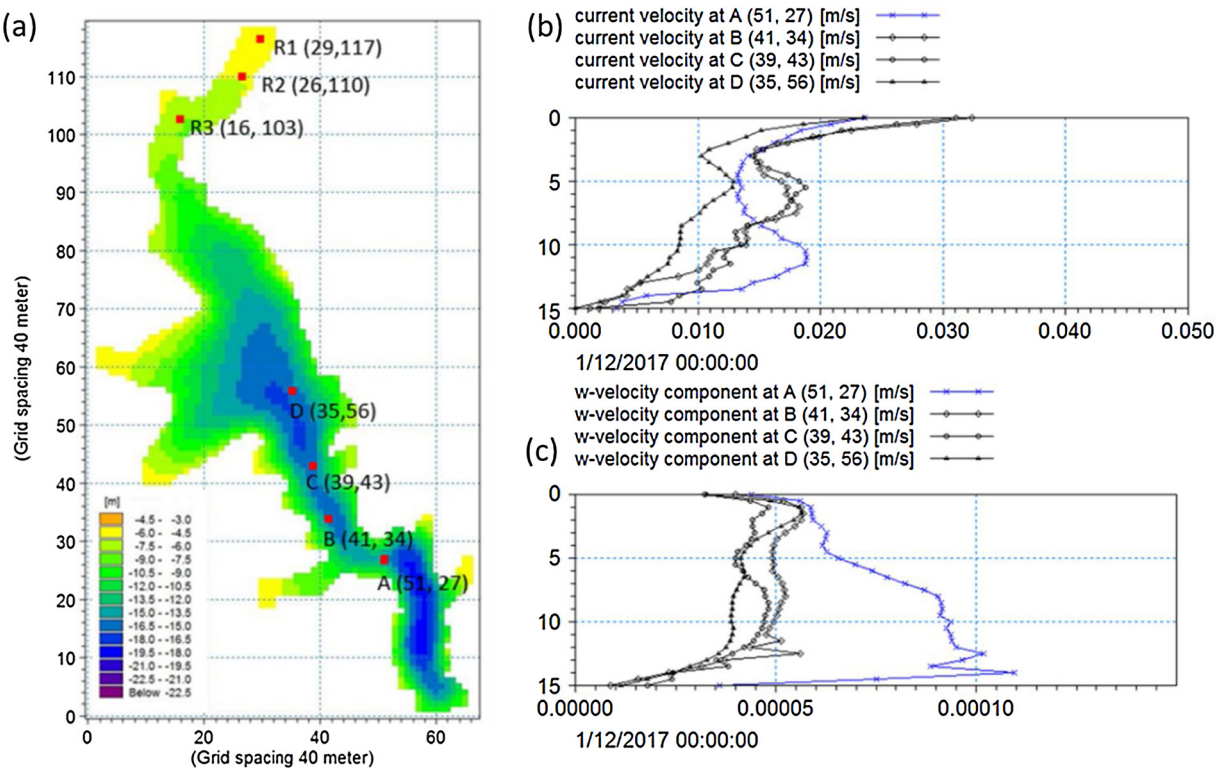

Fig. 11. (a) The coordinates of spots A, B, C, D, R1, R2, and R3; (b) the vertical profile of mean absolute current velocity of spots A, B, C, and D in December 2017; and (c) the vertical profile of the mean absolute vertical velocity component of spots A, B, C, and D in December 2017.

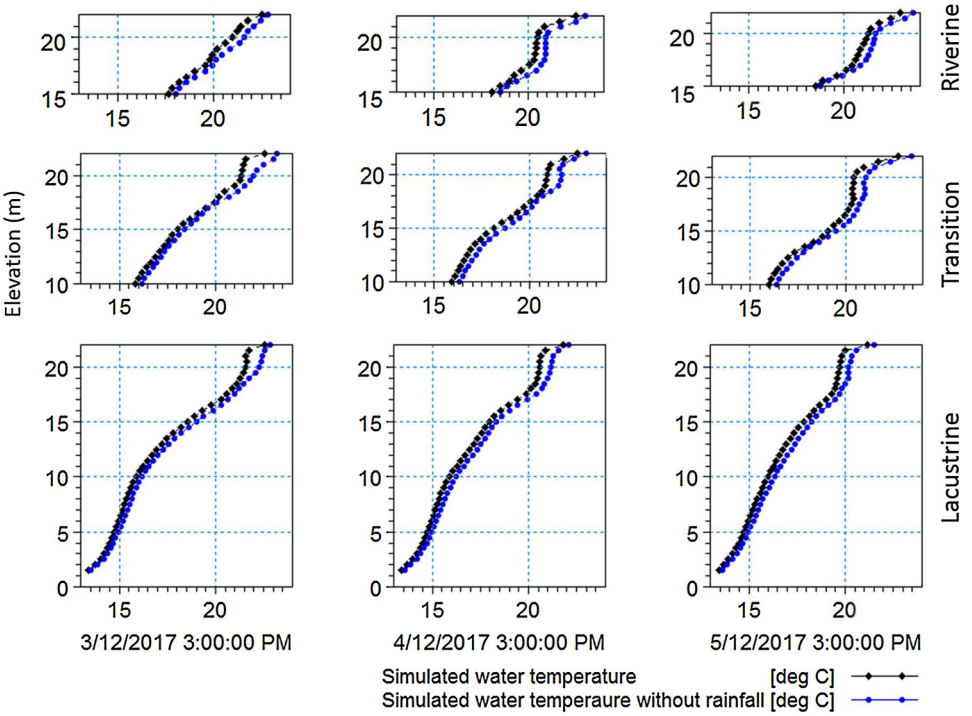

Fig. 12. Simulated vertical profiles of water temperature from the original model and no-rainfall model in the riverine, transition, and lacustrine zones.

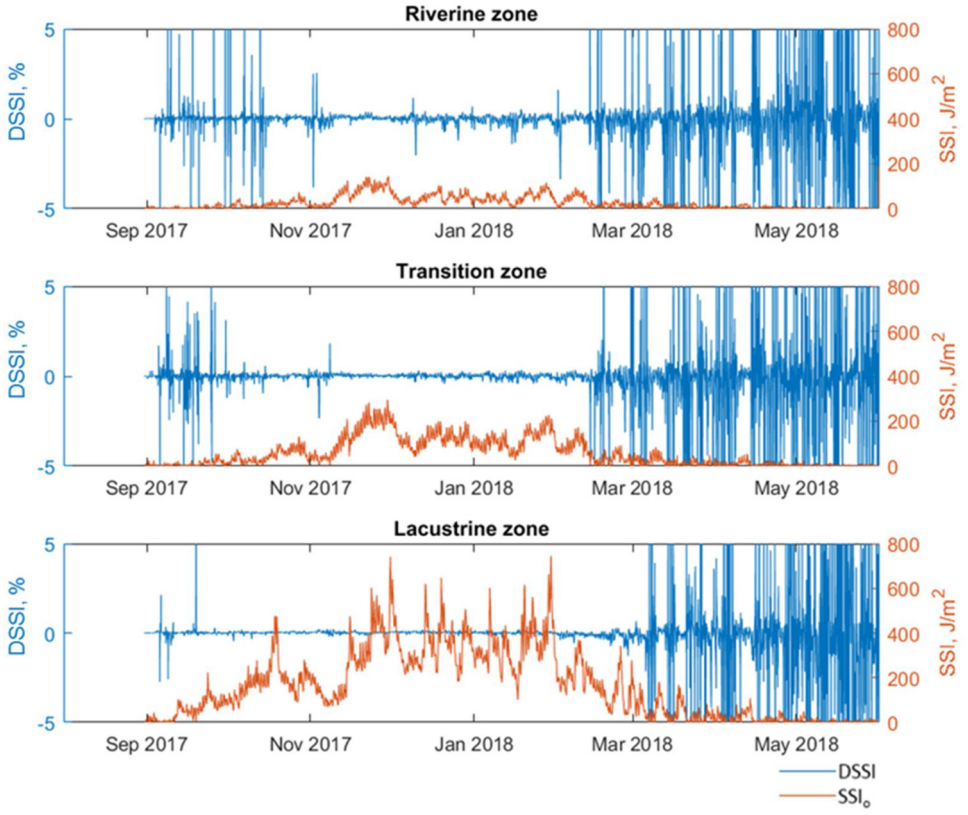

Fig. 13. Time series of the DSSI and SSIo in the riverine, transition, and lacustrine zones.

Reservoir required a 3D simulation of the flow dynamics. To represent the aforementioned roles, the simulated flow conditions were represented using velocity vectors. The contour of the horizontal water-temperature distribution and velocity vector at various depths are presented in Figs. 18 and 19. To minimise the wind effect, the selected dates were 18th December 2017 and 7thJanuary 2018, which were both during the stratification period and had daily average wind speeds of 0.644 m/s and 0.723 m/s, respectively, in nonuniform directions.

Fig. 18(a) presents a typical overflow plume, in which a high water-temperature inflow dominates the direction of surface currents and drives the upper currents uniformly to flow downstream. Moreover, the deeper-layer currents at depths of 4 m (b) and 8 m (c) presented an opposite flow directions to the surface currents. The current at 4 m was chaotic, but that at 8 m was highly consistent. In summary, a warm overflow plume generally replaced the water in the shallow layer and drove the original epilimnion water into the deeper layer during the stratification period in the Tarago Reservoir. Moreover, a circulation formed under the influence of the warm overflow plume, and a noticeable eddy occurred in the interlayer of the circulation. By contrast, as seen in Fig. 19, the cold underflow plume inserted into the deep layer and created a reverse circulation, promoting warm water to float to the epilimnion and leading the high-temperature surface water in the downstream to backflow into the upstream. To demonstrate the entire structure of the circulation, Fig. 20 displays the simulated current and temperature distributions at cross-sections X1–X2.

The broader definition of inflow suggests that the differences in heat exchange between riverine zones and the deeper zone play a considerable role in the flow dynamics. The response of water temperature in the riverine zone is faster than that in the deeper zones when reservoirs gain or lose the same amount of heat. The higher water temperature in the riverine regions (Fig. 18(a)) presented a heat input to the waterbody, and that in the lacustrine zone (Fig. 19(a)) indicated a heat loss to the waterbody. Fig. 21 displays the variations in local air temperature during the study period. The overflow occurred when the daily air temperature maintained steady growth, and the underflow occurred when air temperatures took a significant and sudden drop.

In conclusion, the different reactions to the heat input or output among riverine, transition, and lacustrine zones created the overflow or underflow without wind, and either the overflow or underflow created vertical circulations in the reservoir. The overflow enhanced the stability of stratification because the warmer water floated and relatively cold water moved to a deeper layer. However, the circulations created by underflow provided much heat to the middle and deep layers through the underflow and created partial mixing in the transition and lacustrine zones of the reservoir. Although previous studies have proven that wind is the main force driving circulations (Falconer et al., 1991; Gibbs et al., 2016; He et al., 2011), our findings indicated that overflow or underflow caused by the different responses between riverine and lacustrine zones to heat exchange also contributed to the circulation and had opposite effects on the thermal structure of the reservoir; however, wind maintained a dominant role with regards to circulation potential.

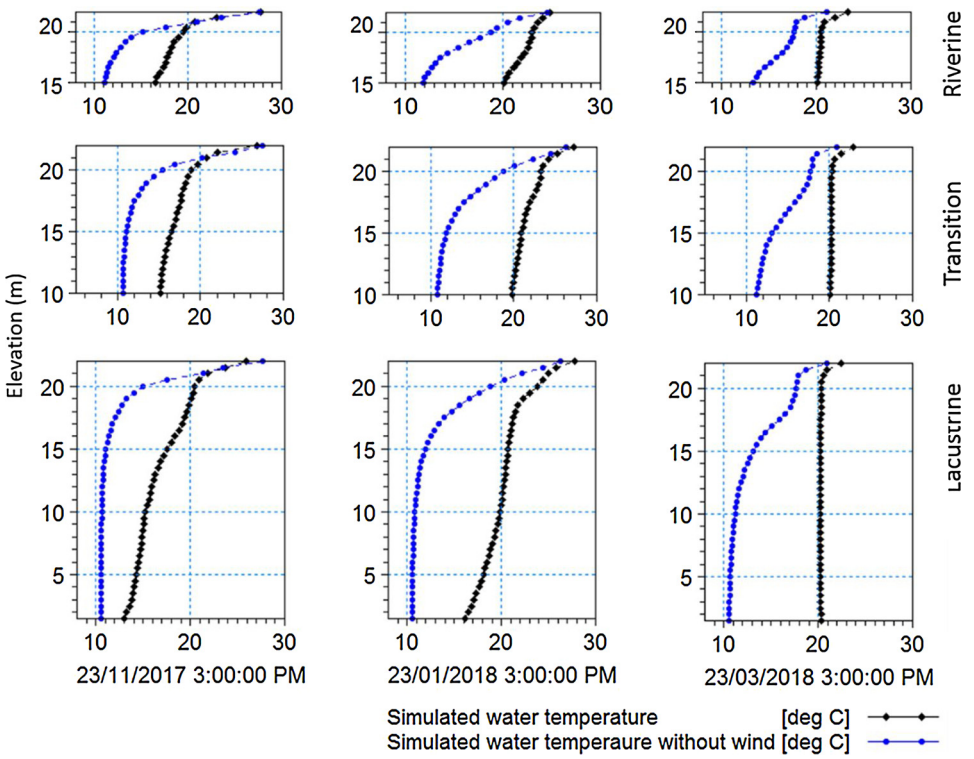

Fig. 14. Simulated vertical profiles of water temperature from the original model and no-wind model in the riverine, transition, and lacustrine zones.

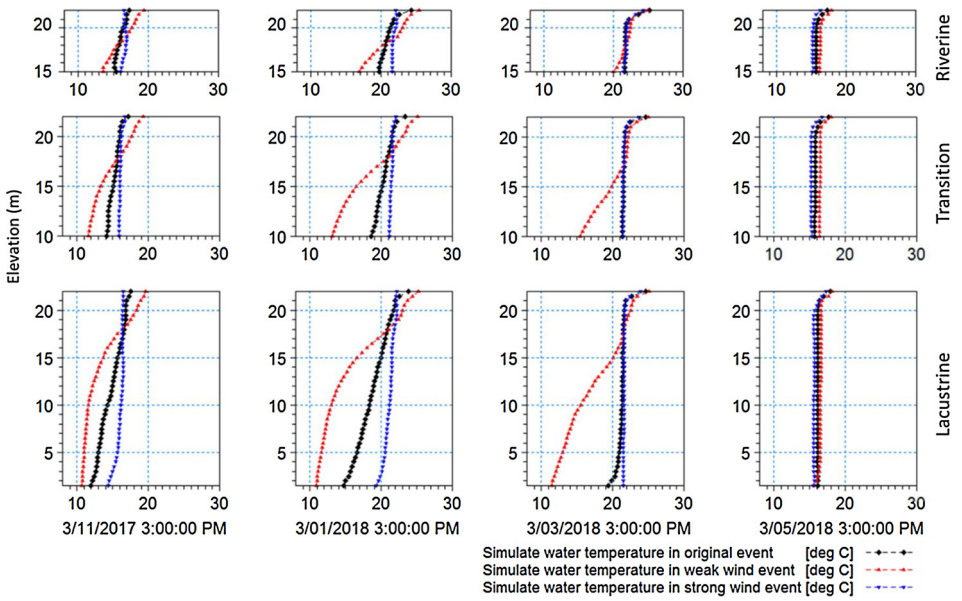

Fig. 15. Simulated vertical profiles of water temperature from the original, weak wind, and strong wind events in the riverine, transition, and lacustrine zones.

5. Conclusions

A 3D hydrodynamic model of the Tarago Reservoir was developed using the MIKE 3 Flow Model. Water level and temperature measured by the VPS were used to calibrate and validate the model, and the model achieved good accuracy.

With the simulations of the 3D numerical model, the analysis of the thermal structure of the reservoir extended from a single

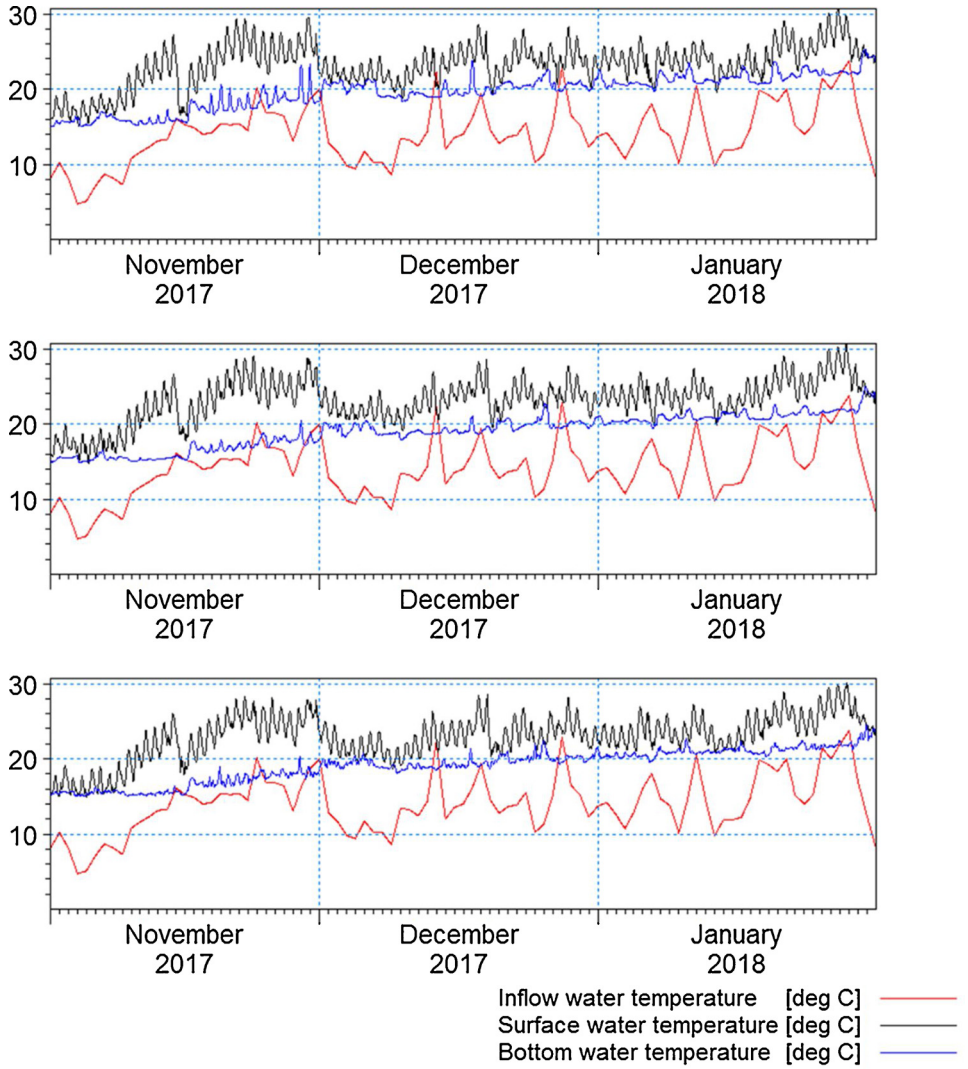

Fig. 16. Time series of water temperature of inflow and R1, R2, and R3 in the riverine zone from November 2017 to February 2018.

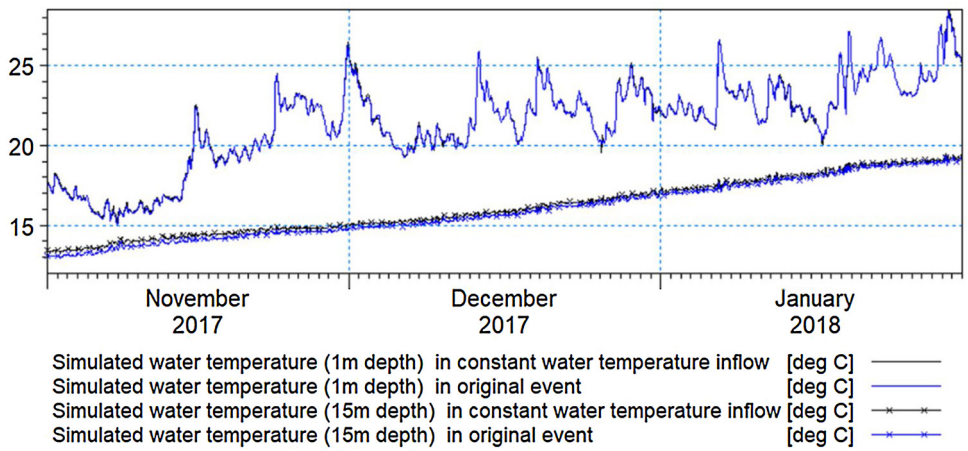

Fig. 17. Time series of simulated water temperature from the original model and constant inflow water temperature model in the lacustrine zones.

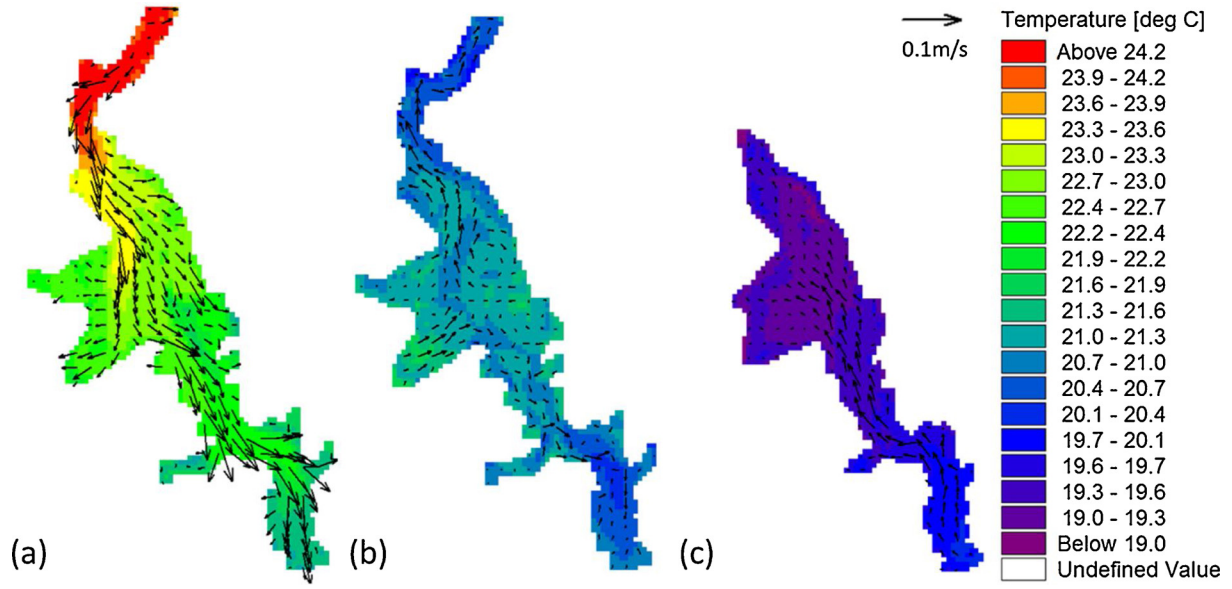

Fig. 18. Simulated warm overflow (m/s) and temperature (°C) distributions on 18th December 2017 at (**a**) surface; (**b**) 4 m below surface; (**c**) 8 m below surface.

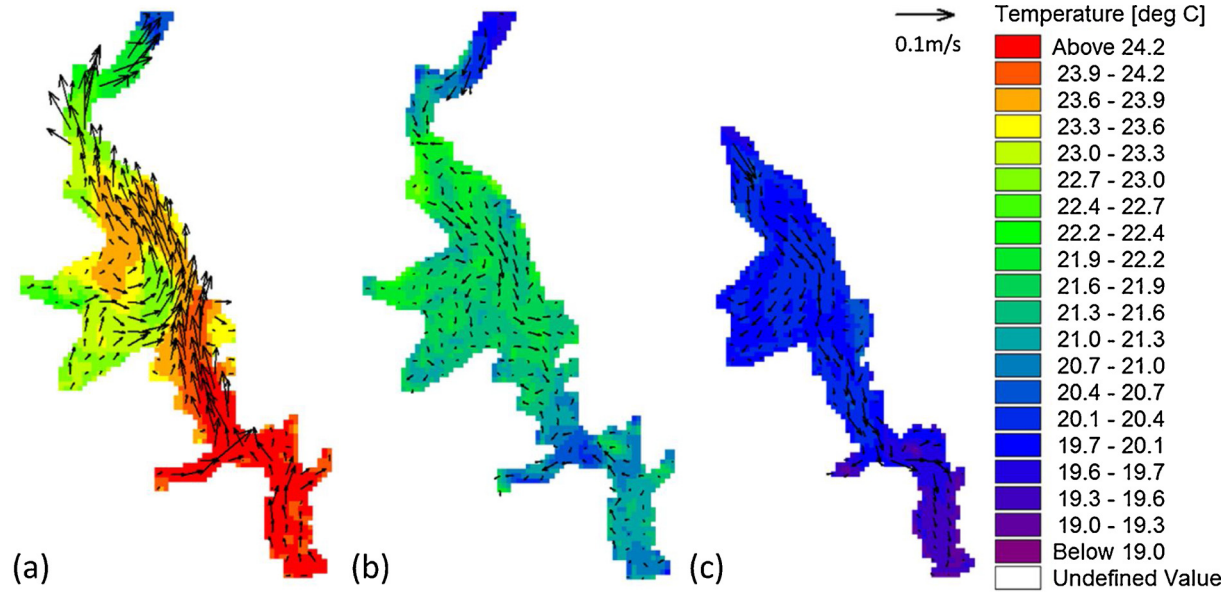

Fig. 19. Simulated cold underflow (m/s) and temperature (°C) distributions on 7th January 2018 at (**a**) surface; (**b**) 4 m below surface; (**c**) 8 m below surface.

observation point to the entire reservoir. The vertical water temperature patterns of riverine, transition, and lacustrine zones showed the longitudinal difference in thermal structure. The introduction of the SSI helped to quantify the thermal structure of the entire research domain, revealing the effects of water depth, seasonal change, and special morphometric changes on stratification stability. The contribution of rainfall to the lake stratification was minimal; instead, the vital roles of wind condition in the formation and destruction of thermal stratification and also heat storage were revealed through adjusting wind conditions. The overflow and underflow related to the air temperature created inverse circulations that significantly influenced the stratification.

The development and application of our 3D hydrodynamic model not only enhanced the understanding of the thermal structure of the Tarago Reservoir but also provides a feasible method for discovering the role of external factors in the thermal structure of waterbodies. Future work will focus on using the developed model to assess manganese transport in the Tarago Reservoir, because manganese spikes are regularly recorded in the raw water of the TWTP during turnover events.

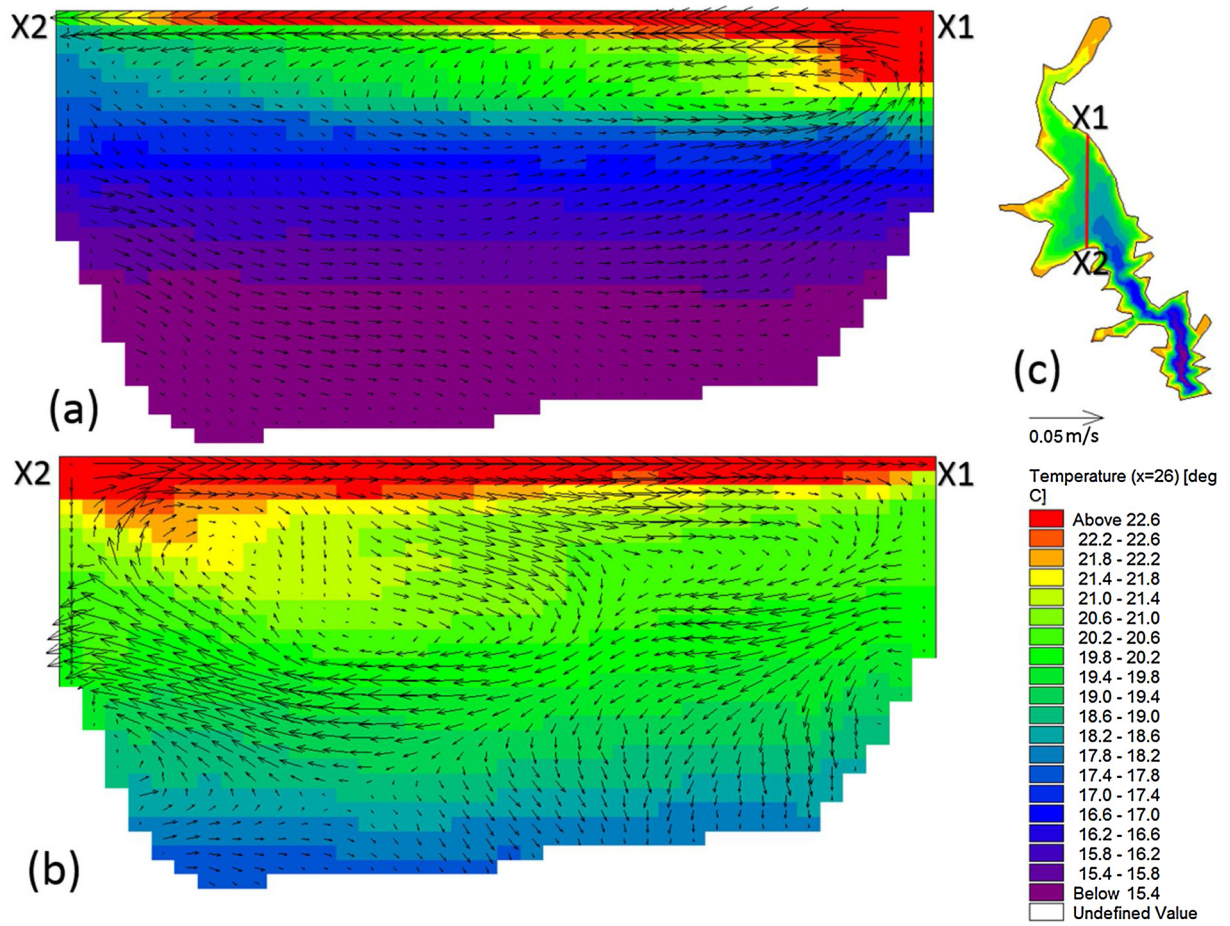

Fig. 20. Warm overflow event on 18th December 2017 **(a)** and cold underflow event on 7th January 2018 **(b)** at cross section X1-X2 **(c)**.

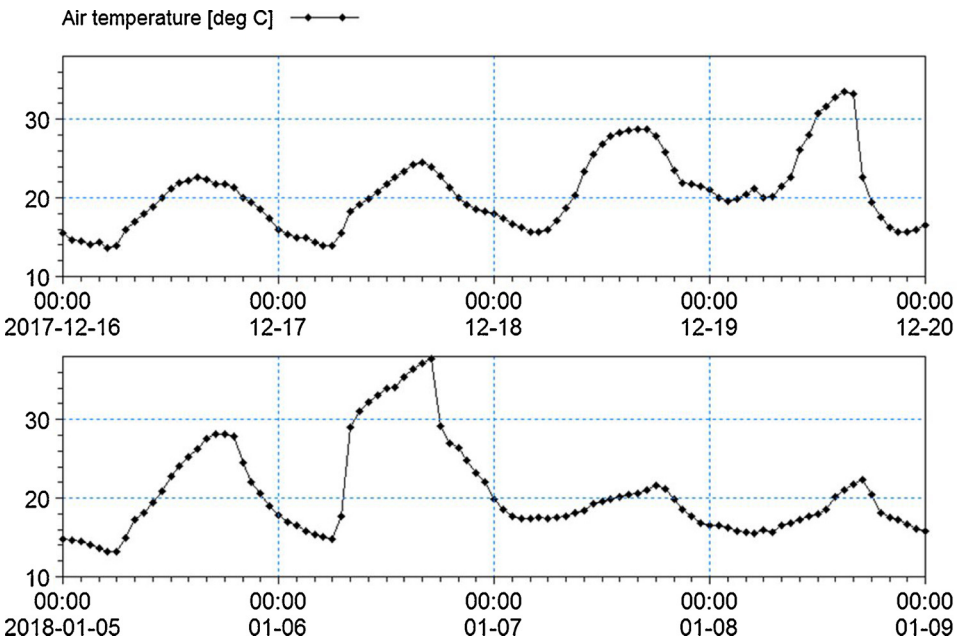

Fig. 21. Time series of air temperature near the overflow (18/12/2017) and underflow (07/01/2018) events.

Funding

This research was partially funded by the Australian Government through the Australian Research Council (ARC LP160100217).

CRediT authorship contribution statement

Fuxin Zhang: Conceptualization, Methodology, Software, Validation, Formal analysis, Writing - original draft. **Hong Zhang:** Conceptualization, Methodology, Writing - review & editing. **Edoardo Bertone:** Conceptualization, Validation, Writing - review & editing. **Rodney Stewart:** Conceptualization, Writing - review & editing. **Charles Lemckert:** Writing - review & editing. **Kathy Cinque:** Data curation.

Declaration of Competing Interest

The authors declare no conflict of interest.

Acknowledgements

This research work was conducted with the technical and financial support of Melbourne Water and Griffith University. We acknowledge the use of meteorological data and water temperature from the Vertical Profile System of Melbourne Water and Australian Bureau of Meteorology.

Appendix A. Supplementary data

Supplementary material related to this article can be found, in the online version, at doi:https://doi.org/10.1016/j.ejrh.2020.100699.

References

Antonopoulos, V.Z., Gianniou, S.K., 2003. Simulation of water temperature and dissolved oxygen distribution in Lake Vegoritis, Greece. Ecol. Modell. 160 (1–2), 39–53.
Australian Bureau of Statistics, 2016. 2016 Census QuickStats.
Bertone, E., Stewart, R.A., Zhang, H., O'Halloran, K., 2015. Analysis of the mixing processes in the subtropical Advancetown Lake, Australia. J. Hydrol. 522, 67–79.
Boehrer, B., Schultze, M., 2008. Stratification of lakes. Rev. Geophys. 46 (2).
Chao, X., Jia, Y., Shields Jr., F.D., Wang, S.S., Cooper, C.M., 2010. Three-dimensional numerical simulation of water quality and sediment-associated processes with application to a Mississippi Delta lake. J. Environ. Manage. 91 (7), 1456–1466.
Dargahi, B., Setegn, S.G., 2011. Combined 3D hydrodynamic and watershed modelling of Lake Tana, Ethiopia. J. Hydrol. 398 (1-2), 44–64.
DHI, 2017. User Guide of MIKE3: Estuarine and Coastal Hydraulics and Oceanography, Hydrodynamic Module.
Falconer, R., George, D., Hall, P., 1991. Three-dimensional numerical modelling of wind-driven circulation in a shallow homogeneous lake. J. Hydrol. 124 (1–2), 59–79.
Gibbs, M., Abell, J., Hamilton, D., 2016. Wind forced circulation and sediment disturbance in a temperate lake. N. Z. J. Mar. Freshw. Res. 50 (2), 209–227.
Han, B.-P., Armengol, J., Garcia, J.C., Comerma, M., Roura, M., Dolz, J., Straskraba, M., 2000. The thermal structure of Sau Reservoir (NE: Spain): a simulation approach. Ecol. Modell. 125 (2–3), 109–122.
He, G., Fang, H., Bai, S., Liu, X., Chen, M., Bai, J., 2011. Application of a three-dimensional eutrophication model for the Beijing Guanting Reservoir, China. Ecol. Modell. 222 (8), 1491–1501.
Hebbert, B., Patterson, J., Loh, I., Imberger, J., 1979. Collie river underflow into the Wellington reservoir. J. Hydraul. Eng. 105 (5), 533–545.
Helfer, F., Zhang, H., Lemckert, C., 2009. Evaporation Reduction by Windbreaks: Overview, Modelling and Efficiency. Urban Water Security Research Alliance Technical Report No. 11.
Helfer, F., Zhang, H., Lemckert, C., 2011. Modelling of lake mixing induced by air-bubble plumes and the effects on evaporation. J. Hydrol. 406 (3–4), 182–198.
Henderson-Sellers, B., 1986. Calculating the surface energy balance for lake and reservoir modeling: a review. Rev. Geophys. 24 (3), 625–649.
Horiuti, K., 1987. Comparison of conservative and rotational forms in large eddy simulation of turbulent channel flow. J. Comput. Phys. 71 (2), 343–370.
Hostetler, S., Bartlein, P., 1990. Simulation of lake evaporation with application to modeling lake level variations of Harney-Malheur Lake, Oregon. Water Resour. Res. 26 (10), 2603–2612.
Imberger, J., Hamblin, P.F., 1982. Dynamics of lakes, reservoirs, and cooling ponds. Annu. Rev. Fluid Mech. 14 (1), 153–187.
Imboden, D.M., Wüest, A., 1995. Mixing mechanisms in lakes. Physics and Chemistry of Lakes. Springer, pp. 83–138.
Ji, Z.-G., 2017. Hydrodynamics and Water Quality: Modeling Rivers, Lakes, and Estuaries. John Wiley & Sons.
Kheirabadi, H., Noori, R., Samani, J.M., Adamowski, J.F., Ranjbar, M.H., Zaker, N.H., 2018. A reduced-order model for the regeneration of surface currents in Gorgan Bay, Iran. J. Hydroinform. 20 (6), 1419–1435.
Kirillin, G., 2010. Modeling the impact of global warming on water temperature and seasonal mixing regimes in small temperate lakes. Boreal Environ. Res. 15 (2), 279–293.
Kirillin, G., Shatwell, T., 2016. Generalized scaling of seasonal thermal stratification in lakes. Earth Sci. Rev. 161, 179–190.
Lawson, R., Anderson, M.A., 2007. Stratification and mixing in Lake Elsinore, California: an assessment of axial flow pumps for improving water quality in a shallow eutrophic lake. Water Res. 41 (19), 4457–4467.
Legates, D.R., McCabe Jr., G.J., 1999. Evaluating the use of "goodness of fit" measures in hydrologic and hydroclimatic model validation. Water Resour. Res. 35 (1), 233–241.
León, L.F., Lam, D.C.-L., Schertzer, W., Swayne, D.A., Imberger, J., 2007. Towards coupling a 3D hydrodynamic lake model with the Canadian regional climate model: simulation on Great Slave Lake. Environ. Model. Softw. 22 (6), 787–796.
Lessin, G., Raudsepp, U., Stips, A., 2014. Modelling the influence of major baltic inflows on near-bottom conditions at the entrance of the Gulf of Finland. PLoS One 9 (11), e112881.
Li, Y., Zhang, Q., Ye, R., Yao, J., Tan, Z., 2018. 3D hydrodynamic investigation of thermal regime in a large river-lake-floodplain system (Poyang Lake, China). J. Hydrol. 567, 86–101.

Ma, T., Liu, W.-h., Song, C., Cheng, W., 2009. Application of MIKE3 in prediction analysis of the water temperature of reservoir. Power Syst. Clean Energy 2.
MacKay, M.D., Neale, P.J., Arp, C.D., Domis, L.D.S., Fang, X., Gal, G., et al., 2009. Modeling lakes and reservoirs in the climate system. Limnol. Oceanogr. 54 (6part2), 2315–2329.
Magee, M.R., Wu, C.H., 2017. Response of water temperatures and stratification to changing climate in three lakes with different morphometry. Hydrol. Earth Syst. Sci. 21 (12), 6253–6274.
Noori, R., Asadi, N., Deng, Z., 2019. A simple model for simulation of reservoir stratification. J. Hydraul. Res. 57 (4), 561–572.
Patterson, J.C., Imberger, J., 1989. Simulation of bubble plume destratification systems in reservoirs. Aquat. Sci. 51 (1), 3–18.
Read, J.S., Hamilton, D.P., Jones, I.D., Muraoka, K., Winslow, L.A., Kroiss, R., et al., 2011. Derivation of lake mixing and stratification indices from high-resolution lake buoy data. Environ. Model. Softw. 26 (11), 1325–1336.
Schmidt, W., 1928. Über temperatur and Stabilitätsverhaltnisse von seen. Geogr. Ann. 10, 147–177.
Smith, S., Banke, E., 1975. Variation of the sea surface drag coefficient with wind speed. Q. J. R. Meteorol. Soc. 101 (429), 665–673.
Sokolova, E., Pettersson, T.J., Bergstedt, O., Hermansson, M., 2013. Hydrodynamic modelling of the microbial water quality in a drinking water source as input for risk reduction management. J. Hydrol. 497, 15–23.
Sundaram, T.R., Rehm, R.G., 1971. Formation and maintenance of thermoclines in temperate lakes. AIAA J. 9 (7), 1322–1329.
Torriano, F., Picher, P., Chaaban, M., 2012. Numerical investigation of 3D flow and thermal effects in a disc-type transformer winding. Appl. Therm. Eng. 40, 121–131.
Tuan, N., Hamagami, K., Mori, K., Hirai, Y., 2009. Mixing by wind-induced flow and thermal convection in a small, shallow and stratified lake. Paddy Water Environ. 7 (2), 83–93.
Tucker, W.A., 1982. Surface heat fluxes from lake Ontario: further verification of lake thermal model. Water Resour. Res. 18 (1), 77–82.
Vo, N.D., Gourbesville, P., 2016. Application of deterministic distributed hydrological model for large catchment: a case study at Vu Gia Thu Bon catchment, Vietnam. J. Hydroinform. 18 (5), 885–904.
Webb, B., Nobilis, F., 1997. Long term perspective on the nature of the air water temperature relationship: a case study. Hydrol. Process. 11 (2), 137–147.
Weisman, R.N., Brutsaert, W., 1973. Evaporation and cooling of a lake under unstable atmospheric conditions. Water Resour. Res. 9 (5), 1242–1257.
Willmott, C.J., 1981. On the validation of models. Phys. Geogr. 2 (2), 184–194.
Xuan, L., Tinglin, H., Weixing, M., Xin, S., Haihan, Z., 2015. Effects of rainfall patterns on water quality in a stratified reservoir subject to eutrophication: implications for management. Sci. Total Environ. 521, 27–36.
Young, S., 2009. Tarago Water Treatment Plant Operations Manual.
Yu, Y., Zhang, H., Lemckert, C., 2014a. Numerical analysis on the Brisbane River plume in Moreton Bay due to Queensland floods 2010–2011. Environ. Fluid Mech. 14 (1), 1–24.
Yu, Y., Zhang, H., Lemckert, C., 2014b. Salinity and turbidity distributions in the Brisbane River estuary, Australia. J. Hydrol. 519, 3338–3352.
Zhang, H., Chan, E.-S., 2003. Modeling of the turbulence in the water column under breaking wind waves. J. Oceanogr. 59 (3), 331–341.